International Journal of Mechanical Sciences 193 (2021) 106173

Contents lists available at ScienceDirect

International Journal of Mechanical Sciences

journal homepage: www.elsevier.com/locate/ijmecsci

Predicting mechanical properties of 316L stainless steel subjected to SMAT: A sequential DEM-FEM investigation

Yongmei Zhang [a], Gwénaëlle Proust [a], Delphine Retraint [b], Huamiao Wang [c], Yixiang Gan [a,d,*]

[a] School of Civil Engineering, The University of Sydney, Sydney, NSW 2006, Australia
[b] ICD-LASMIS, Université de Technologie de Troyes (UTT), CNRS FRE 2019, 12 Rue Marie Curie, 10010 Troyes, France
[c] State Key Laboratory of Mechanical System and Vibration, School of Mechanical Engineering, Shanghai Jiao Tong University, Shanghai, 200240, China
[d] The University of Sydney Nano Institute (Sydney Nano), The University of Sydney, NSW 2006, Australia

ARTICLE INFO

Keywords:
SMAT
DEM-FEM framework
residual stress
surface roughness
plastic deformation
stainless steel

ABSTRACT

Surface mechanical attrition treatment (SMAT) is a specialized cold working method that is used to induce compressive residual stresses and to refine crystalline grains at the surface of metal components. This technique is increasingly employed in different industries, and the control and optimization of the method require a fundamental understanding and an accurate process modelling. In this study, a numerical modelling approach capable of accurately predicting the residual stress and plastic deformation during SMAT was developed by combining discrete element method (DEM) and finite element method (FEM). In the proposed framework, the spatial and statistic distributions of impact positions, angles and velocities from DEM simulations are utilized in the FEM simulations. The effects of treatment duration, shot number, shot size and impact angle distribution on residual stresses, plastic deformation and roughness of the treated component are investigated. The numerical results are compared with available experimental data with good agreements. The proposed numerical method demonstrates capabilities to establish the linkages between processing parameters and material properties during SMAT treatment.

1. Introduction

Extensive studies indicate that the strength/hardness of polycrystalline metals is greatly increased with a substantial reduction in grain size to nanoscale [1-4]. Free-standing nano-grained (NG) metals usually exhibit a very limited ductility. However, an NG layer at the surface and a coarse-grained (CG) substrate of the same metal with a gradient grain-size transition between them has higher strength and plasticity comparable to that of the CG substrate [5]. Surface nanocrystallization of CG metals by means of severe plastic deformation techniques is now a feasible option to improve the performance of metallic parts [6-9]. Improvements in fatigue life, wear resistance, bio-compatibility and corrosion resistance have been shown through the creation of nanograins and compressive residual stresses in the near surface region [1,5,10-12]. Surface mechanical attrition treatment (SMAT) [13-16], a simple, yet flexible and cost-effective surface nanocrystallization method, has been widely used to improve mechanical properties of metals, such as 316L stainless steel, which is a widely used alloy for biomedical applications [17-20]. This process generates a nanocrystalline layer at the surface of the treated material [2,21-24], which, due to the large fraction of grain boundaries and beneficial compressive residual stresses, presents extraordinary strength, fatigue life and wear resistance [25-30]. During SMAT, the surface of the target is repeatedly impacted by multi-directional spherical particles with high speed, causing the surface to undergo severe plastic deformation [3,31] and resulting in a progressive grain refinement at the surface [32,33]. So far, the mechanisms for nanocrystalline generation during SMAT [34] and the properties of SMATed material [35] have been well researched by experimental investigations. However, the deformation history during SMAT and the effects of processing parameters on the resulted properties of the target are still unclear. Therefore, an accurate and reliable numerical model for predicting the SMAT process is still urgently required.

The microstructure, surface topography and mechanical properties of treated materials depend on the severe plastic deformation history during SMAT [31]. Some researchers attempted to investigate the resulting strain state using analytical studies or computational modelling to avoid the time and cost related to the trial-and-error approach. Chaise et al. [36] calculated the average plastic strain tensor using semi-analytical method and then transferred it into finite element method (FEM) to predict the deformation and residual stresses. Yin et al. [37,38] proposed an analytical algorithm cooperating with FEM to simulate the strain distribution and surface topography of material after SMAT. The analytical methods involved multiple linear interpolating the result of FEM simulation, during which the error and inaccuracy were enlarged.

* Corresponding author.
E-mail address: yixiang.gan@sydney.edu.au (Y. Gan).

https://doi.org/10.1016/j.ijmecsci.2020.106173
Received 20 July 2020; Received in revised form 22 October 2020; Accepted 24 October 2020
Available online 27 October 2020
0020-7403/

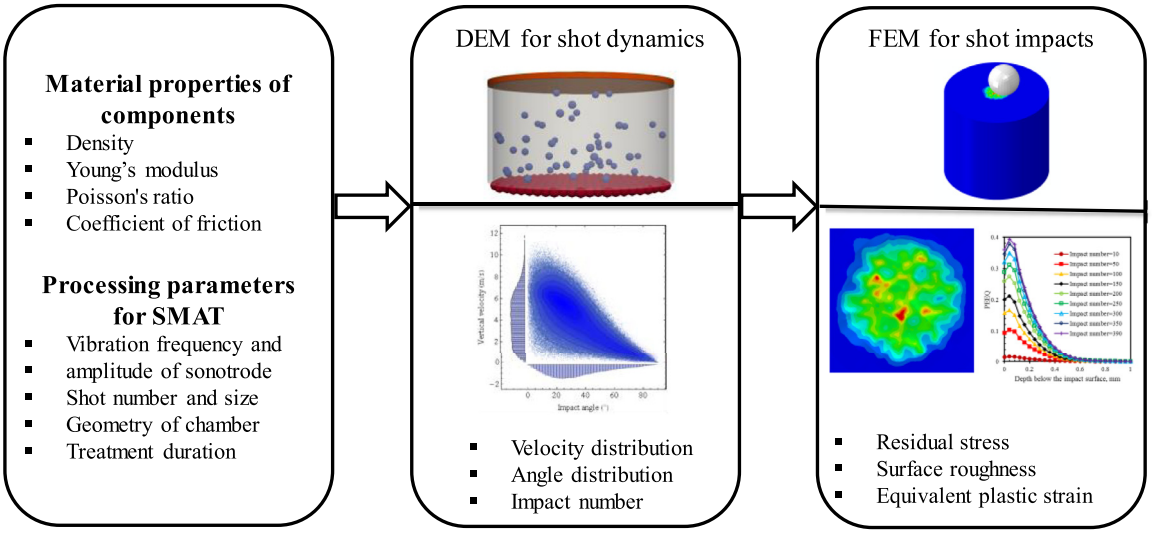

Fig. 1. Schematic of the proposed sequential DEM-FEM modeling procedure for SMAT treatment.

FEM can also be directly used for predicting the distribution of residual stresses, plastic deformation and surface roughness. Zhang et al. [39] conducted single shot impact simulations to calculate the indent size with varying shot diameter and impact angle. Multiple shot particles simulation was also carried out to determine the residual stress and vertical displacement at the surface of the target. Meguid et al. evaluated the effect of shot velocity, size and aspect ratio on the plastic zone and residual stress by using the single impact model [40] and the multiple impact model [41]. The multiple impact models studied uniformly distributed positions and prearranged sequences. However, this assumption cannot define the random nature of SMAT process and thus failed to simulate the actual SMAT process. Pham et al. [42] and Cao et al. [43] developed full-coverage multiple-impact models to impose the positions of shot particles. Gangaraj et al. related the simulation to actual coverage [44] and simulated the surface nanocrystallization [45]. Though the impact locations were random to achieve full coverage, the impact angles were all vertical to the target [42] or uniformly distributed from 0° to 90° [43].

Modelling SMAT process is very complex as it involves the interactions of a metallic surface with many impacts for which information regarding position, velocity and impact angles are uncertain. Discrete element method (DEM), which handles complex and random interactions of particles, can be used to investigate the resulting impact locations, impact velocities and impact angles [46]. With the detailed and accurate knowledge of the realistic shot impact information, the strain state at different depth can be determined by FEM numerical modelling. When investigating the result of shot peening, some researchers coupled DEM simulation to FEM simulations and made them communicate with each other at every time step [47]. The concurrent DEM-FEM coupling method is physically motivated but required extensive computations. Moreover, the different length scale in DEM and FEM created some difficulties regarding the dimensions of the target for DEM simulations. On the other hand, in a sequential scheme, shot stream in shot peening is first simulated with DEM, and the shot velocities or contact force as well as the impact positions were sequentially transferred into FEM simulation [48]. Different from shot peening, the impact angles in SMAT are not unidirectional, and the impact angles are relevant to vertical impact velocities [49]. How to input the joint distribution between impact angle and vertical impact velocity is one of the difficult problems to solve.

Shot size, impact velocity distribution, impact angle distribution, shot number and treatment duration are the input parameters needed in FEM simulation. According to our previous study [49], the joint distribution of impact velocity and impact angle is affected by the processing parameters used during SMAT, such as the vibration amplitude and frequency of the sonotrode and the geometrical features of the chamber. The treatment duration and shot number can be reflected by impact number in FEM. Thus, the effect of processing parameters of SMAT is ascribed to the effect of impact number, the joint distribution of impact angle and vertical impact velocity, and shot size. The microstructure, surface topography and mechanical properties of SMATed materials can be reflected by equivalent plastic strain (PEEQ), vertical displacement and compressive residual stress. PEEQ is recognized as a common favorable parameter to reflect the nanograins generation [45,50]. Vertical displacement can be used to calculate the surface roughness. Compressive residual stress is beneficial to prevent the occurrence of cracking [36] and improve fatigue life [10,51,52], stress corrosion resistance and load carrying capacity [53] of materials.

The main objective of this paper is to propose a sequential DEM-FEM modelling method, illustrated in Fig. 1, for predicting SMAT process for 316L. The responses of the treated material include compressive residual stress, surface roughness, and PEEQ. The modelling work described in this article has three parts. The first part aims at describing how to impose initial impact velocities and positions, determined by DEM simulations, as input in the FEM model. The second part considers the single impact model by discussing material properties, geometries, mesh method, mesh size convergence, contact properties, boundary conditions and damping factor. The third part consists of the multiple impact model and considers the effects of treatment duration, shot number, velocity distribution, impact angle distribution and shot size on the roughness, PEEQ and residual stresses of the treated material.

2. Numerical method

The proposed sequential DEM-FEM modeling procedure is a modification of that introduced by Tu et al. [48]. First, under the specified material properties of components and the processing parameters for SMAT, the shot dynamics is simulated in LIGGGHTS to obtain the distributions of impact velocity, impact position and impact angle of shot, and the impact number at given treatment duration. The extracted shot dynamics were then imported into ABAQUS/explicit for simulating the response of the target in terms of residual stress, surface roughness and PEEQ. Fig. 1 schematizes the DEM-FEM modeling procedure.

2.1. DEM-FEM coupling

DEM records the motion of each single shot and its interaction with the target, sonotrode, chamber and other shot. The position, velocity and acceleration of each shot are updated incrementally, with short time

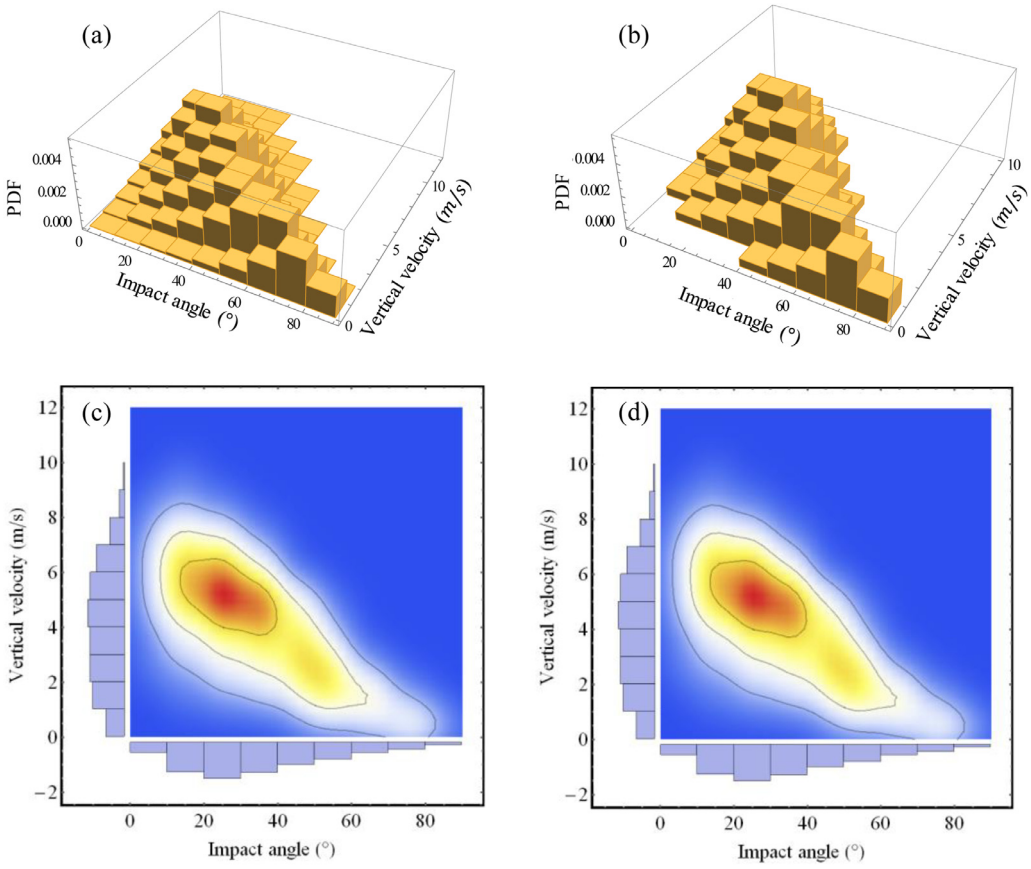

Fig. 2. The histogram frequency distribution of impact angle and vertical velocity from (a) the original dataset from DEM simulation and (b) subsample used for FEM input; The density distribution of impact angle and vertical velocity from (c) the original DEM simulation and (d) subsample used for FEM input.

intervals. The input processing parameters for the DEM simulation contain: the size and number of the shot, the vibration amplitude and frequency of the sonotrode, and the height and radius of the chamber. In DEM simulation, the position and critical impact velocity of the shot are continuously monitored and output. The output is what is used as the input in the FEM simulations.

The detailed DEM modelling method is presented in our previous work [49]. We know that the distribution of the vertical velocity is dependent on the impact angle, while the tangential velocity is independent of the impact angle and follows a normal distribution. The spatial distribution of impact locations is uniform on the target and independent to the impact angle and vertical impact velocity.

As in our DEM simulations, the treatment duration is as long as 150 s and the accumulated impact number reached up to 270,000 over the target with a radius of 35 mm. In order to meet the population distribution, at least 5,000 impacts are needed, which is time consuming and impractical in FEM simulations. Since the impact number is large and the impact area is also large in DEM simulations, the challenge of this work is to link DEM to FEM. The proposed methodology consists in using with a reduced impact number and a smaller impact area while ensuring the sample distribution is consistent with the full population from the DEM study.

In this work, because of the cost of simulation time, a reasonable impact number to be simulated in the FEM model is 200. These 200 impacts should reflect and keep the same distributions of the full population. From our DEM simulations, the case study, r20d346 (see Ref. [46] for details), is chosen. This case study has the following SMAT process parameters: vibration frequency of sonotrode, 20kHz; vibration amplitude of sonotrode, 25 μm; shot diameter, 3 mm; shot number, 50; distance of target- to- sonotrode; 38 mm; root mean square roughness of the sonotrode surface Rq, 0.6 mm. Using the full data obtained from the DEM simulation, the histogram frequency distribution of the full population for the treatment duration of 150 s is extracted after the steady state. The data is then discretized using bin widths of 10 degrees and 1m/s, respectively, as shown in Fig. 2(a). The histogram frequency of each bin times 200 (the impact number we planned to import into FEM), and then round the result, we can obtain histogram list. The histogram frequency distribution of FEM input sample, see Fig. 2(b), can be obtained from the histogram list. By comparing the density distributions of impact angles and vertical impact velocity from the full population (see Fig. 2(c)) and the FEM input sample (see Fig. 2(d)), we can say the FEM input sample almost keep the same distribution of the full population.

The histogram list of vertical impact velocity V_y, and impact angle θ for FEM input has been obtained according to the above method. Then we need to assign the three velocity components, V_x, V_y, V_z, and two impact position components, x and y, to each shot. Because vertical impact velocity V_z and impact angle θ were two dependent variables, another independent variable was selected as azimuth angle, as shown in Fig 3(a). According to Fig. 3(b), then the two tangential velocities V_x and V_y could be expressed as

$$V_x = V_z \tan\theta \cos\varphi, \tag{1}$$

$$V_y = V_z \tan\theta \sin\varphi. \tag{2}$$

Since the spatial distribution of impact position, as well as the azimuth angle were uniform and independent to impact angle and vertical impact velocity, we generated the 195 impact positions and azimuth angle data using RandomVariate command in Mathematica.

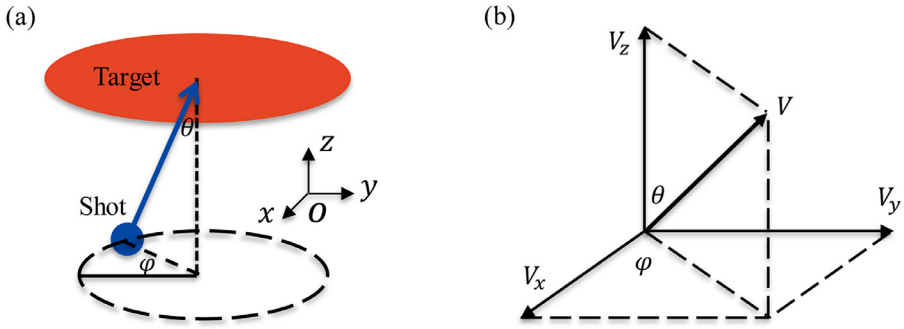

Fig. 3. (a) The definition of impact angle θ and azimuth angle ϕ; (b) The velocity decomposition to calculate two horizontal velocities V_x and V_y.

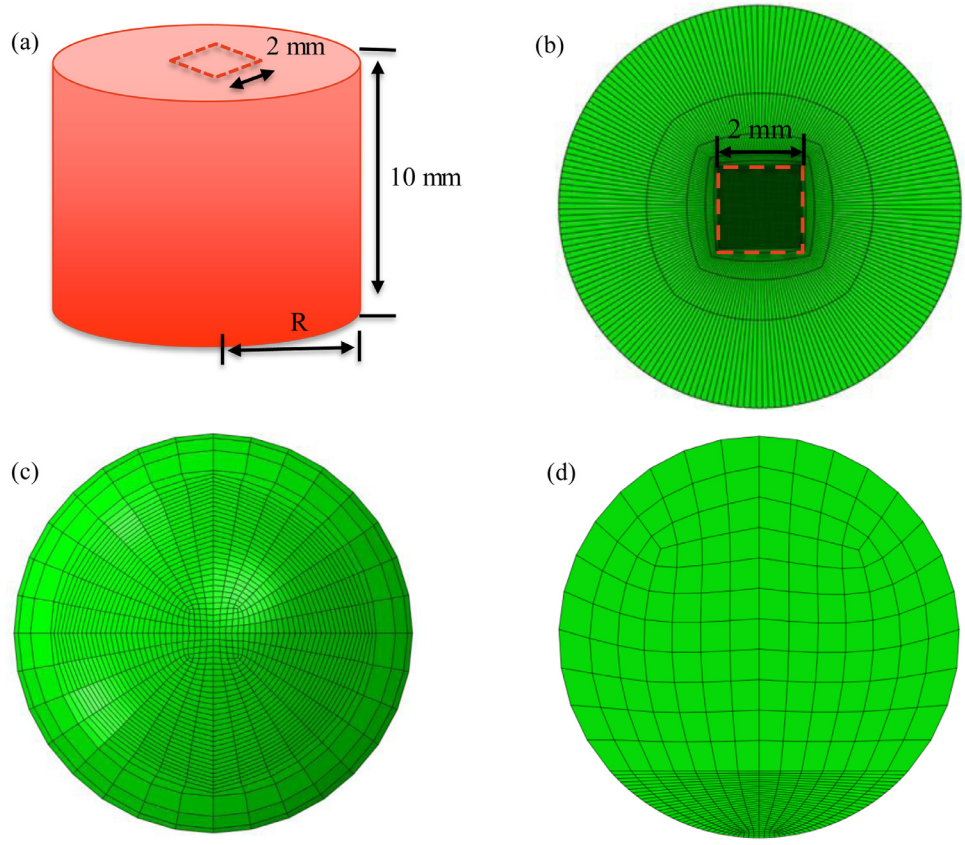

Fig. 4. (a) The schematic view of the target in finite element simulation model; (b) mesh refinement of the target at the impact area. The red squares in (a) and (b) represent the boundary of fine mesh region; (c) the bottom view and (d) sectional view of fine mesh at the bottom of the shot.

2.2. Single impact model

3D finite element models for single impact and multiple impacts are developed in this work. The single impact model is used to optimize the simulation parameters, such as mesh size and damping factor. The multiple impact model is utilized to determine the proper target size and region of interest (ROI) size, and then to simulate the process of SMAT.

The 3D FE models are built using the commercial finite element software ABAQUS/ Explicit 6.14. To avoid the edge effect from the impact wave, the target in our simulation is considered as a cylinder. The height of the cylinder should be large enough to prevent the interference from the bottom boundary. Meguid et al. [41] indicates that a height, H, at least twice the value of the shot diameter, D, is suitable for different shot velocities and multi-indentation problems. In our model, we use shot diameter D = 3, 4 and 5 mm. Thus, we adopt a target height of 10 mm. The ROI, which has a finer mesh than the rest of the target, is chosen as cuboid rather than a cylinder, see Fig. 4(a), to ensure mesh uniformity and to simplify the delineation of the impact area. The fine mesh zone, which has a dimension of $2 \times 2 \times 1$ mm^3, is located in the center of the cylinder surface. Shot is modelled as spherical body. To avoid the rotational inertia difference resulting from the oblique impacts, we model the full shot in our simulation.

As indicated in Fig. 4(b), the mesh closed to the impact area is much finer to increase the resolution of the plastic strain distribution beneath the surface in the fine mesh region and gradually the mesh becomes coarser away from the fine mesh region to reduce the computation time. As shown in Fig. 4(c & d), the bottom region of the shot has the same mesh size as the impact area of the target to avoid sharp corner on the spherical surface during contact. The bottom of the target is constrained against all freedom degrees. The initial impact velocity and position of shot are predefined. The element C3D8R, which is an 8-node linear brick element with reduced integration (with one integration point) and hourglass control, is used to discretize both the target and the shot. General contact is used as the criteria of contact and interface contact elements are introduced using the penalty algorithm with an isotropic coulomb friction coefficient of 0.2, which is a typical values for dynamic contact [54,55].

By comparing rigid shot and elastic shot, we have found that the deformable shot leads to a decrease in the residual stress and the depth of

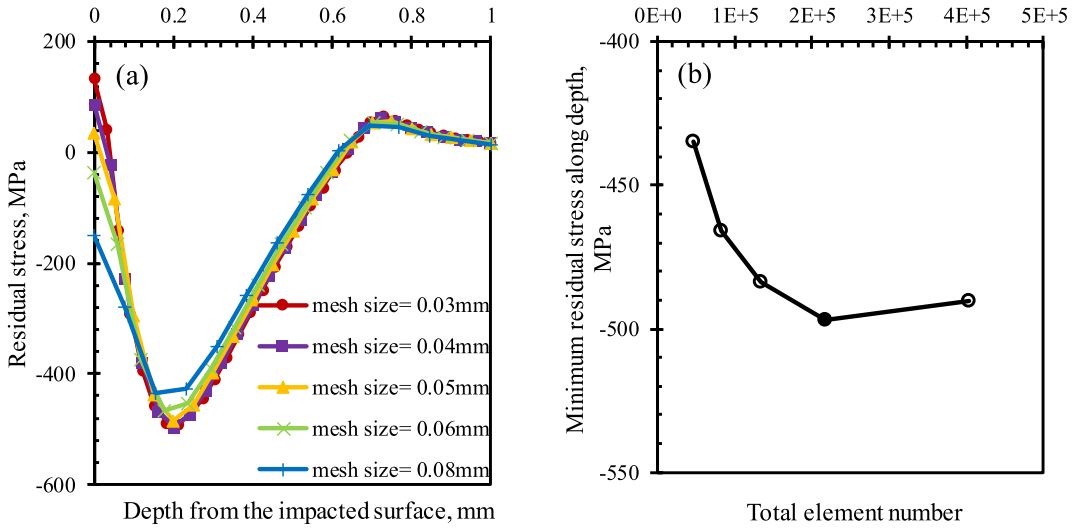

Fig. 5. (a) Residual stress profiles along the depth beneath the impact surface for different mesh sizes of the target; (b) Minimum residual stress for different total element numbers used in the model.

compressive zone of the target. A considerable part of the impact energy is absorbed by the deformable shot. Thus, an isotropic elastic material property is used to simulate the shot behavior, with an elastic modulus of 200 GPa, a density of 7900 kg/m^3, and a Poisson's ratio of 0.29. For the properties of the target, strain rate plays an important role in modeling the distribution of residual stress and plastic strains during shot impact. Meguid et al. [41] studied the effect of strain rate by using rate insensitive and rate sensitive materials, and the result showed that the strain rate effect increased the maximum compressive residual stress and decreased the depth of the plastic zone. Thus, it is vital that the constitutive model used to model the deformation behavior of the target reflects the dependence of the hardening law with the plastic strain, but also describes the strain rate sensitivity of the yield strength. The Johnson-Cook (J-C) material hardening behavior, which expresses the flow stress as a function of plastic strain, strain rate and temperature, is used here to model the plastic behavior of the target. The model parameters used for the simulations in this paper are the same as the ones used in our previous work [49].

Some model parameters, such as the mesh size, the radius of the target and the size of the region of interest (ROI), are optimized to achieve a better accuracy and solution stability, while maintaining appropriate computational time. The radius of the target should be large enough to prevent interference from the surrounding boundary. The size of the ROI should be reasonable to contain all the information of impacts on the target.

Convergence tests are conducted using different mesh sizes in the finer mesh zone. The mesh size of both the target and the shot are kept the same as explained previously. The results of this convergence study, see Figs. 5(a) and (b), indicate that by using a mesh size of 0.04mm, which corresponds to a total element number of 164000, the model can simulate the shot impacting process in a time effective way. Therefore, the mesh size of 0.04mm is used for the rest of the work.

In our work, the simulations are carried out such that a ball impacts the target surface once the previous ball has rebounded and the residual oscillations from the previous impacts have almost dissipated. To achieve that goal, appropriate damping parameters are introduced to prevent unnecessary long post-impact residual oscillations. If these residual oscillations are not reduced greatly before the next impact occurs, they would accumulate resulting in solution instability. As indicated in Ref. [41,56,57], the material damping is introduced as

$$C = \alpha M + \beta \tag{3}$$

where C is the damping matrix, M is the mass matrix, and K is the stiffness matrix. The mass proportional damping coefficient, α, is effective for low-frequency oscillations, while the stiffness proportional damping coefficient, β, is effective for high-frequency oscillations. Referring to Ref. [57], the stiffness proportional damping coefficient, β, is set as 0 s^{-1}. According to the ABAQUS Analysis User's Manual [56], the damping factor is given by

$$\alpha = 2\omega_0\xi \tag{4}$$

where ξ is the corresponding damping parameter, and ω_0 is the lowest frequency. It can be determined by

$$\omega_0 = \sqrt{\frac{k}{m}} = \frac{1}{H}\sqrt{\frac{E}{\rho}} \tag{5}$$

where E is the target Young's modulus, and ρ is the target density, and H is the target height. After a number of trial simulations, the mass proportional damping factor coefficient is chosen as 515687.1 s^{-1}, corresponding to the model damping factor $\xi = 0.5$. Fig. 6 shows the evolution of the vertical velocity of the impact point on the target surface, without and with using a damping parameter. The residual oscillations are nearly dissipated after 10 μs, thus, the following impact will occur at 15 μs after the previous impact.

2.3. Multiple impact model

Python script is a way to automatically accomplish time-consuming and repetitive tasks in ABAQUS by varying parameters of a simulation. To run the multiple impact jobs automatically, a code written in Python is used to specify the locations and initial velocities of the shot. Separate runs are executed for each impact. The deformation and stress state of the target after previous impact are transferred to the target of next impact as an initial state. The effect of each impact on the target can then be investigated in detail. The time and RAM memory savings using this method were demonstrated previously by Ghasemi et al. [53].

Since SMAT generates severe plastic deformations on the impact region, ALE (arbitrary Lagrangian-Eulerian) adaptive meshing is used. ALE adaptive meshing can usually maintain a high-quality mesh throughout a large deformation analysis where severe distortion occurs by allowing the mesh to move independently of the material. The effect of ALE was investigated in our study, and the results showed that ALE had little influence on the simulation results. Therefore, this adaptative meshing technique is used for the multiple impact model.

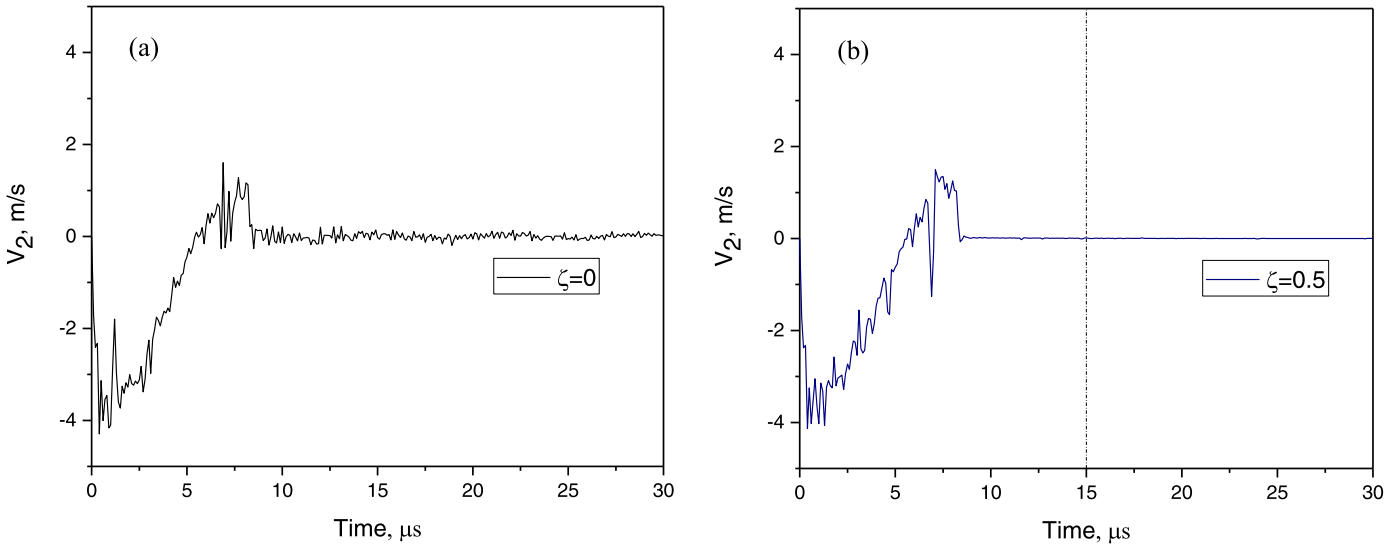

Fig. 6. The vertical velocity of the node at the center of the indentation versus time (a) without using a damping factor and (b) with using a damping factor ξ of 0.5.

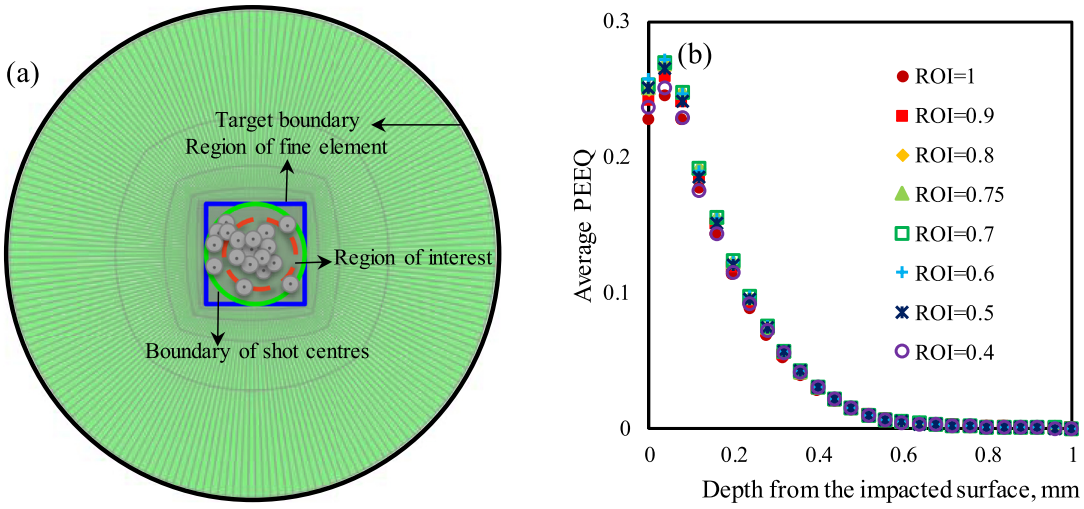

Fig. 7. (a) Schematic view of the different target regions defined in the impact surface of target. The grey circles represent the indents on the target caused by shot impacts; (b) Profiles of the average PEEQ along the depth beneath the impact for different region of interest (ROI). The ROI diameters are listed on the figure and the unit is mm.

In Fig. 7(a), black circle is the boundary of the target. Blue square is the fine mesh region. Green circle is the area containing the impact locations. Red dashed circle is the region of interest (ROI) in which surface displacement, PEEQ and residual stress profiles are calculated. When the size of ROI is large, the edge of the region has low coverage rate, the simulation result is smaller than the average value. When the size of ROI is small, not enough impact are included, which decreases the average simulation result. The size of ROI is first determined. Analyses are conducted in which only the ROI was modified. All other parameters remain unchanged: radius of target surface = 7 mm, length of the region of fine elements = 2 mm, impact positions (shot centers) locate in the circle with radius = 1 mm. Shot diameters were kept constant at d = 3 mm. Fig 7(b) shows the effect of the ROI on the calculated average PEEQ profiles after 200 impacts. The profile is determined by averaging PEEQs in all the elements of the ROI volume, by element layer. Average PEEQ profile is calculated by averaging PEEQ value in two different directions. We see that the maximum PEEQ and surface PEEQ are not influenced by a change in ROI size. As the average indent radius is 0.24 mm, it was decided to choose the radius of ROI as 0.75 mm to avoid the indent vacancies around the boundary of ROI.

The dimensions of the target can have a significant effect on the numerical results. A parametric study is performed to investigate the effects of the target radius on the simulation results. The radius of the target should be sufficiently large to avoid the effects of boundary conditions on the residual stress state in the impact area. For this purpose, Targets with radius from 3 mm to 7 mm were chosen for the simulations. It can be seen in Fig. 8 that the average PEEQ at each depth and the average PEEQ on the ROI surface for target radii 5, 6, and 7 mm are almost identical. Therefore, for the rest of the simulations a target radius of 5mm is used to reduce simulation time.

3. Results and discussion

The residual stress, equivalent plastic strain (PEEQ), surface coverage and surface roughness are extracted from the multiple impact model simulations. The average nodal residual stress and PEEQ at each depth below the impact surface, and the vertical displacement on the ROI of the target are calculated with the Mathematica programming code. As indicated in the Ref. [53], the residual compressive stress distribution is independent of the measuring direction, only one direction is considered.

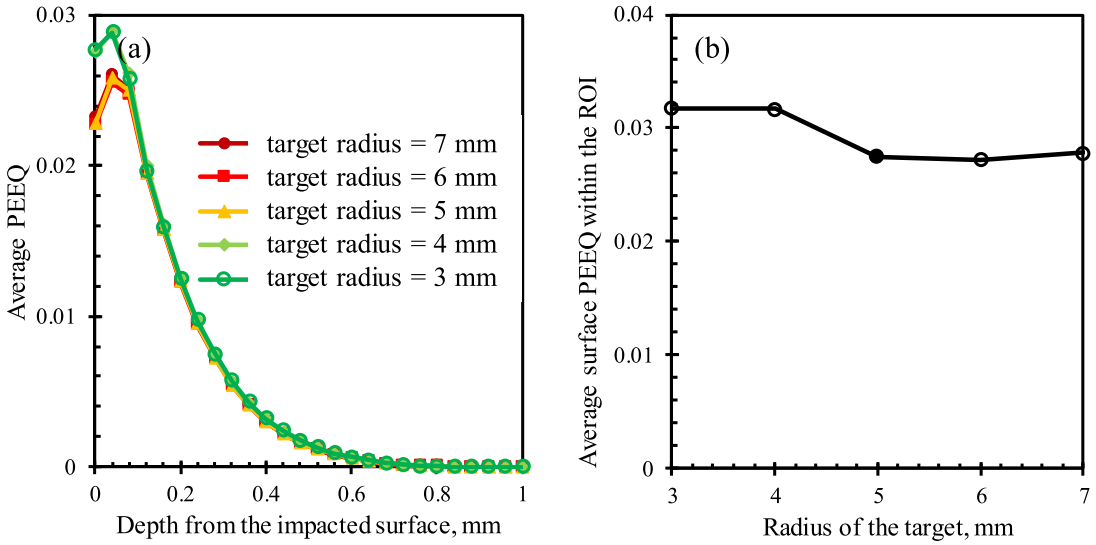

Fig. 8. (a) Profiles of the average PEEQ along the depth beneath the impact surface with different target radii R; (b) Average surface PEEQ within the region of interest (ROI) with different target radii R.

The DEM output needed for the study is the impact coordinates x and y, and the impact velocity components V_x, V_y, and V_z. By varying this data and changing the sequence of the shot for the FEM model, the effects of the impact sequence on the FEM simulation results are investigated. The average PEEQ at each depth and the surface topography are not influenced by the shot sequence after 200 shot impacts.

3.1. Evolution with impact number

Treatment duration and shot number are important factors in SMAT process, and they can be converted to impact number under a given condition of impact intensity. In order to investigate the evolution law of surface roughness, compressive residual stress and PEEQ with treatment duration, 400 impacts were imposed on the target. According to the DEM simulation results, the spatial distribution of the impacts was uniform. The joint distribution of impact velocities and impact angles of the 400 impacts were consistent with the result of the DEM simulations. The shot size to study the effect of treatment duration is 3 mm.

3.1.1. Surface roughness evolution

The surface of the target after SMAT is modified and one way to follow the change is to look at the evolution of the surface roughness. In this study, the root mean square (RMS) roughness R_q is used to describe the surface roughness value. It is expressed as $R_q = \sqrt{\frac{1}{n}\sum_{i=1}^{n} y_i^2}$, where y_i is the vertical displacement of ith data point deducted from the mean vertical displacement for all the data points. The initial roughness is assumed to be $R_q = 0$.

Fig. 9 shows the simulated RMS roughness and the indent coverage of the target as a function of the impact number during the SMAT process. The roughness value increased firstly with the impact number until ~50 impacts (corresponding to a coverage of 93.7%), after which the roughness value began to decrease and then stabilized to a constant value after ~ 100 impacts (corresponding to a coverage of 100%). This phenomenon was also found by Dai et al. [58]. During the increasing roughness stage, the new impacts may occur on the areas already deformed by prior impacts, which increases the vertical displacement. During the decreasing roughness stage, the entire surface has been covered by indents, and the height of the pileup is reduced due to continued impacts. Finally, an equilibrium is achieved between the generation of peaks and the removal of pileups. We compared the roughness simulation results with the experimental data from Dai et al. [58]. Due to the different processing parameters of SMAT between the experiments and our FEM simulations, mainly due to the unknown conversion between the experimental conditions to the impact number, we take the ratio of treatment time to the time when the roughness approaches stable as horizontal axis and the ratio of roughness to the stable roughness value as vertical axis (shown in Fig. 9(b)). The comparison of trends of surface roughness evolution shows a good agreement between simuation and experiments.

3.1.2. Compressive residual stress

Fig. 10(a) shows the average residual stress profile evolution for different impact numbers. Compressive residual stress is created beneath the surface of the target because of local plastic deformation. Moreover, the thickness of the compression stress zone is defined as the depth at which the residual stress approaches zero. As Fig. 10(b) shows, the thickness reaches a first constant value after increasing sharply until 50 impacts (which corresponds to 93.7% coverage as shown on Fig. 9), and it reaches a larger constant value after 175 impacts. The thickness of compressive residual stress zone almost saturates after full coverage. The maximum compressive stress appeared at a depth of roughly 0.08 mm. This maximum value increases exponentially with impact number and then stabilizes after 275 impacts (corresponding to a treatment duration of 228.4s). We compared simulation results of residual stress with the experimental data from Jiang et al. [59]. The residual stress curves between simuation and experiments shows similar tendencies (shown in Fig. 10(c)).

3.1.3. Equivalent plastic strain

Fig. 11(a) shows the average PEEQ profile evolution for different impact numbers. The thickness of the plastic deformation zone is defined as the depth that corresponds to PEEQ = 0.2%. Fig. 11(b) shows the variation of the thickness of the plastic deformation zone as the impact number increases. It can be seen from the figure that the thickness of the plastic deformation zone dramatically increases in the early stage of SMAT and then the rate of increment decreases and, according to the trend, the thickness becomes stable for a high impact number (~ 325 impacts, corresponding to a treatment duration of 269.9s). It is noted that the actual conversion between the number of impacts to the treatment time may differ for different processing conditions, e.g., shot numbers, target area, container size and vibration intensity. However, such a conversion can be obtained by carrying out a DEM simulation with

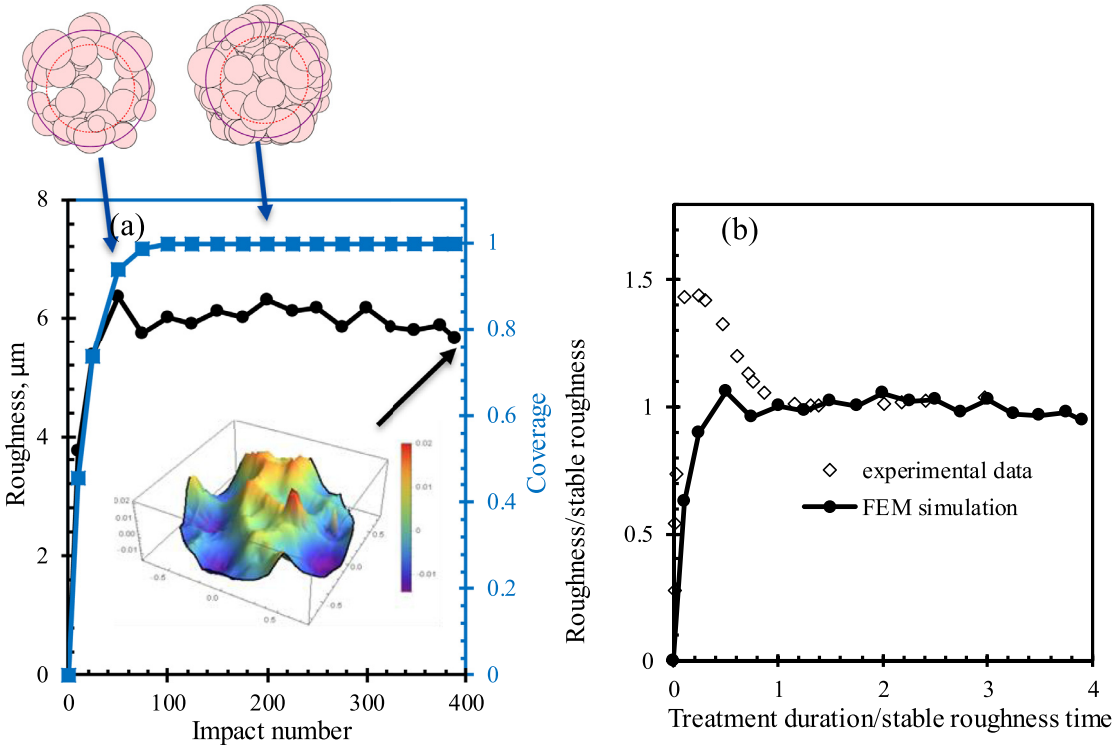

Fig. 9. (a) The evolution of the surface roughness (the black curve) and coverage (the blue curve) with different impact numbers. The pink circles are the impact indents reflecting the coverage evolution. The 3D inset shows the rough surface of ROI after 400 impacts; (b) The comparison between experimental data from Dai et al. [58], shown as scattered points, and FEM simulation for resulting surface roughness. The stable roughness and stable treatment time used for normalization are 80 μm and 60 sec for experimental data, respectively.

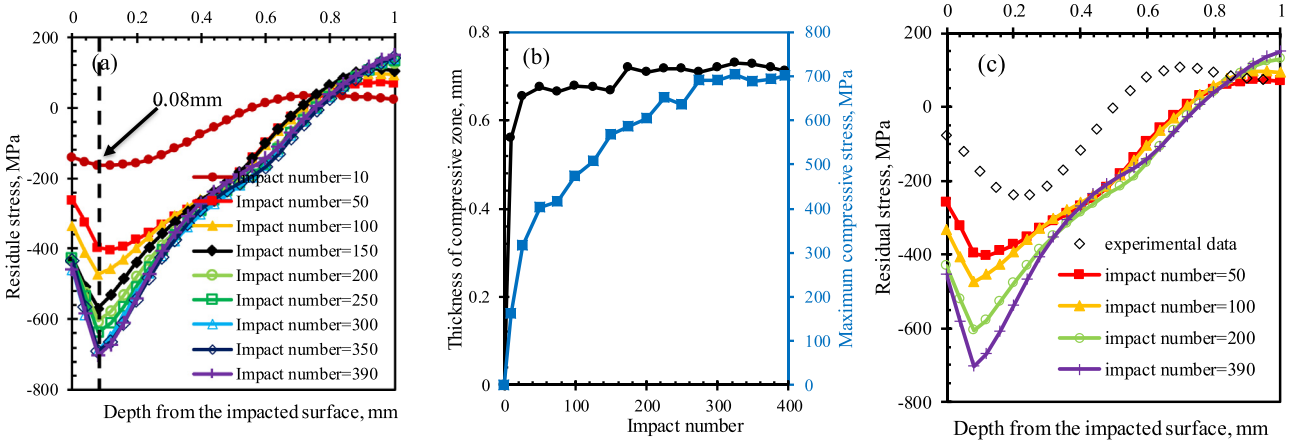

Fig. 10. (a) Profiles of residual stress for different impact numbers; (b) variation of the thickness of compressive stress zone and of the maximum compressive stress as a function of the total impact number and (c) the comparison of residual stress vs. depth between experimental data from Jiang et al. [59], shown as scattered points, and FEM simulation.

the corresponding operational parameters, as shown in [49], to arrive statistical distributions in Fig. 2. The maximum PEEQ is achieved at a depth of around 0.04 mm. The evolution of average surface and maximum PEEQ show an increasing trend but the growth rate is slowing.

According to the Hall-Patch equation [60]: $H_v = 3\sigma_{eq}$, the hardness value along the depth below the processed surface can be calculated according to the Johnson-Cook (J-C) material hardening constitutive equation used in our FEM simulation [49]:

$$\sigma_{eq} = (A + B\varepsilon^n)\left[1 + C\ln\left(\frac{\dot{\varepsilon}}{\dot{\varepsilon}_0}\right)\right]\left[1 - \left(\frac{T - T_0}{T_m - T_0}\right)^m\right] \quad (6)$$

where ε is the plastic strain, $\dot{\varepsilon}$ the strain rate, $\dot{\varepsilon}_0$ the reference plastic strain rate, T the temperature of the target, T_m the melting temperature of the target, T_0 the room temperature, A the yield strength, B the hardening modulus, C the strain rate sensitivity coefficient, n the hardening coefficient and m the thermal softening coefficient. The values of these model parameters for the studied material can be found in the literature [49]. We further compared the hardness simulation result with the experiment data from Yin et al. [27]. Because of the difference of SMAT processing parameters between the experiment and the DEM simulation, we take the ratio of depth to the depth when the hardness approaches stable as horizontal axis and the ratio of hardness to the initial hardness value, H_0, as the vertical axis (shown in Fig. 11(c)). The comparison of trends of hardness evolution shows a good agreement between the simuation and experimental results.

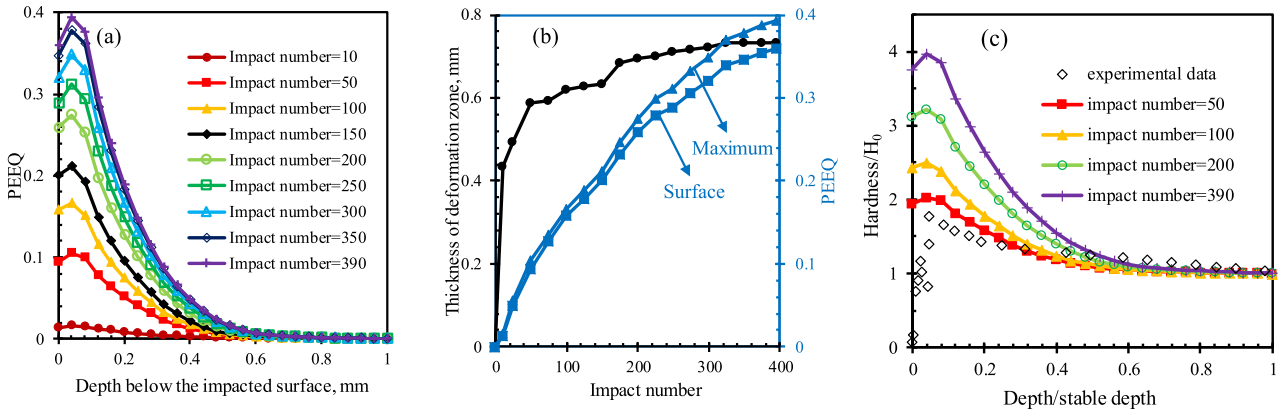

Fig. 11. (a) Profiles of the PEEQ for different impact numbers; (b) variation of the thickness of the deformation zone, and of the maximum and surface PEEQ values as the function of the total impact number and (c) the comparison of hardness ratio between experiment data from Yin et al. [27], shown as scattered points, and DEM simulation. The initial hardness, H_0, and stable depth used for normalization are 3.3 GPa and 0.5 mm for experimental data, respectively.

3.2. The effect of the impact angle distribution

Impact angle distribution plays an important role in the SMAT process. Smaller impact angle causes a rougher surface, which has been verified by experiments conducted by Maliwemu et al.[61] and Nordin et al.[62]. When simulating the process of SMAT, many researchers take the impact angles all vertical to the target (similar to shot peening) [40] or treat the impact angle distribution as uniform from 0° to 90° [41]. From the DEM result, we know the impact angle in SMAT is either equal to 0° or following uniform distribution. As illustrated in Fig. 12(a),

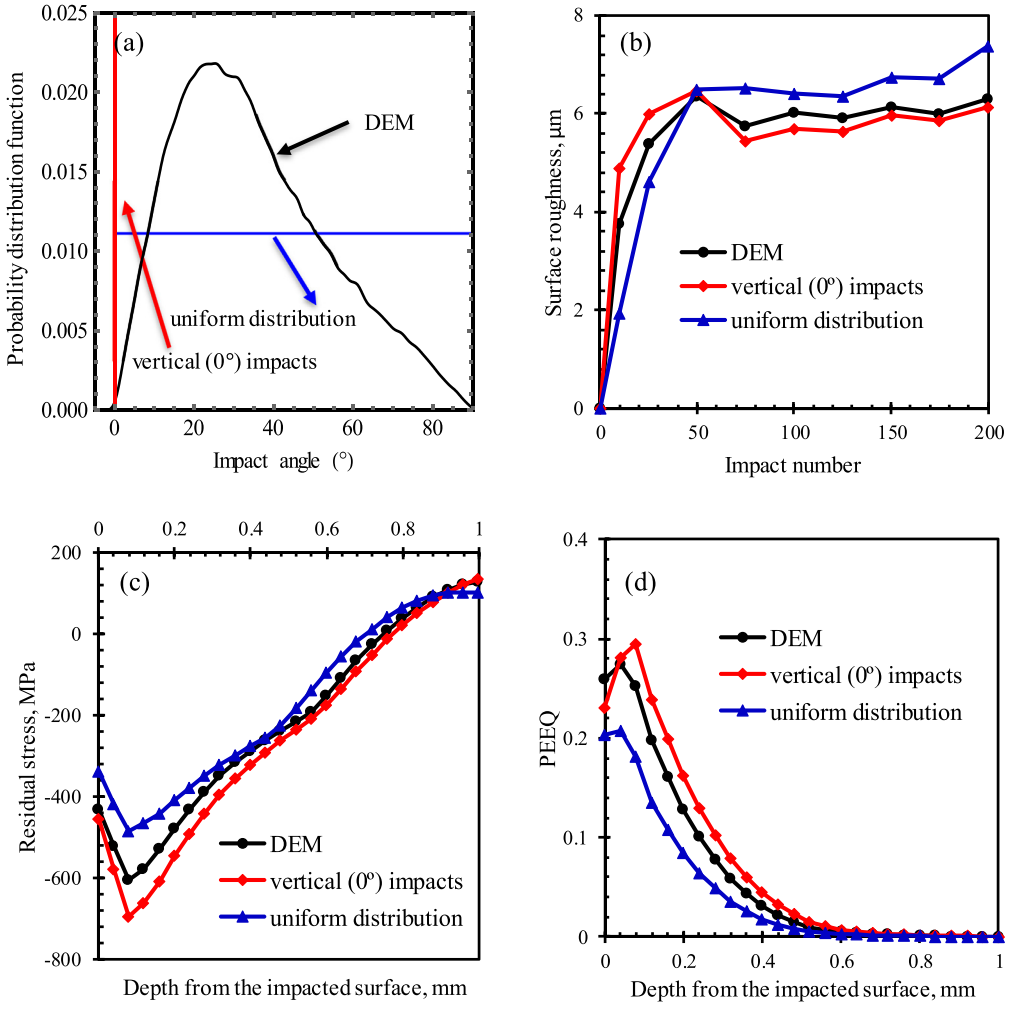

Fig. 12. (a) The different distributions of impact angles from DEM, assuming only vertical impacts and assuming a uniform distribution of the impact angles; (b) Evolution of surface roughness with increasing impact number; Evolution of (c) residual stress and (d) PEEQ with different distributions of impact angles.

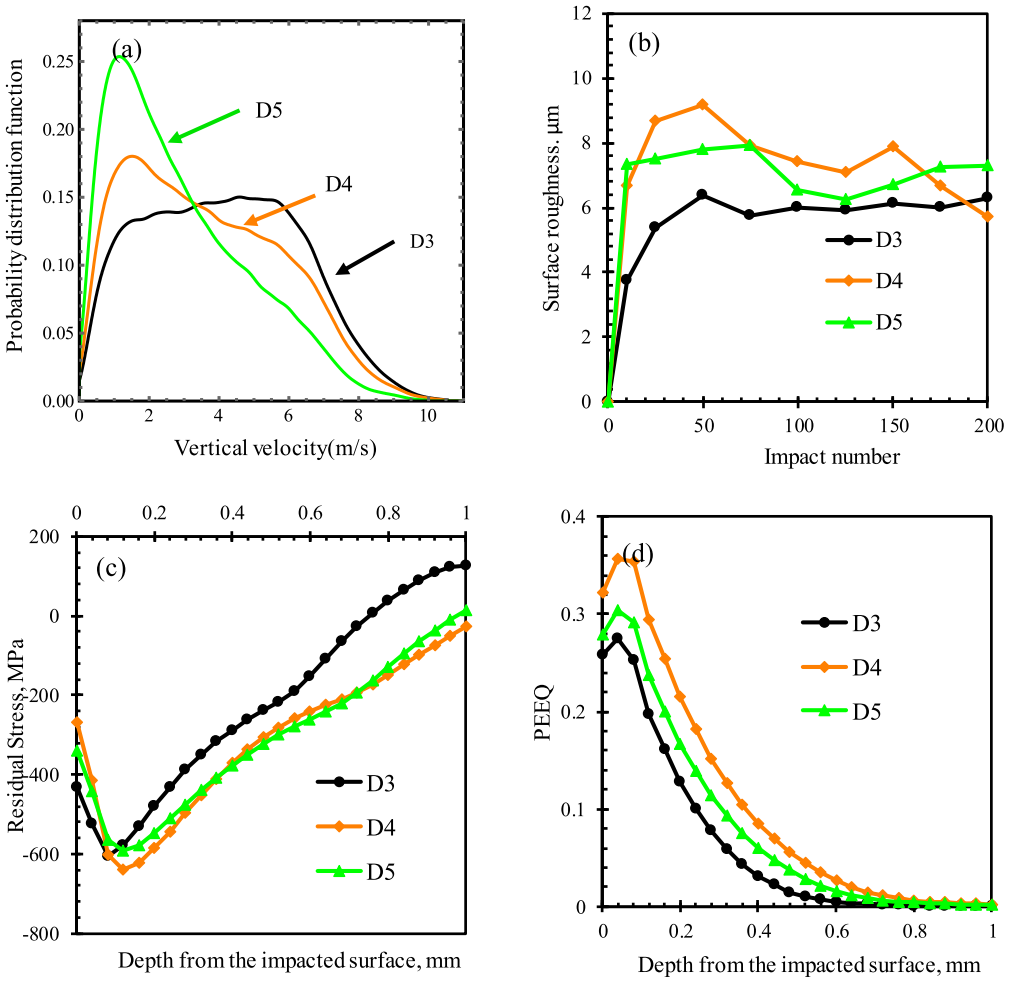

Fig. 13. (a) The distributions of vertical velocity for different shot diameters; (b) the evolution of surface roughness with increasing impact number; the evolution of (c) the residual stress and (d) the PEEQ with different shot diameters.

three cases with different impact angle distribution are investigated. To ensure the total impact kinetic energies are the same during the FEM simulations, the total velocity and position of each impact are kept the same in these three cases.

Fig. 12(b, c & d) show the effect of the impact angle distribution on the simulation results. Fig. 12(b) shows the evolution of the surface roughness with increasing impact number for different impact angle distributions. During the increasing stage of the surface roughness value, the vertical impacts has the greatest increasing rate, followed by the DEM distribution and finally the uniform distribution. For the three different impact angle distribution, the roughness is the same after 50 impacts. After 50 impacts, the surface roughness of both the DEM and vertical impact distributions decreases and then increases slowly. However, the surface roughness of the uniform distribution decreases gradually and then increases again. We can see that the uniform distribution has much higher final surface roughness than the other two distributions, so a broader impact angle distribution range increases the surface roughness after full coverage, which corresponds to ~100 impacts.

Fig. 12(c) shows the evolution of the residual stress with different distributions of impact angles. For the same impact number, the vertical impact distribution results in the largest residual stress and the deepest compressive zone. As the vertical impact distribution has the biggest average vertical velocity component, there seems to be a relation between residual stress and vertical velocity.

Fig. 12(d) shows the evolution of the PEEQ with different distributions of impact angles. For the same impact number, the vertical impact distribution results in the largest PEEQ and the deepest plastic deformation zone. However, the vertical impact distribution has only the second highest surface PEEQ. As a result, we can conclude that larger vertical velocity contributes the compressive deformation, and broader impact angle distribution (or larger average impact angle) causes larger shear deformation on the surface.

3.3. *Effect of the shot size*

According to the DEM simulation result, shot size doesn't influence much the distribution of the impact angle, however, the average vertical velocity decreases with increasing shot size, as illustrated in Fig. 13(a). Fig. 13(b) shows the evolution of the surface roughness with increasing impact number. A diameter of 4 mm results in the maximum surface roughness. The surface roughness is much easier to achieve stable with increasing impact number when the shot size is smaller. For the residual stress evolution, as Fig. 12(c) shows, a diameter of 4 mm results in the maximum compressive residual stress and thickness of compressive zone, however, it has the minimum surface compressive residual stress. For the PEEQ evolution, a diameter of 4 mm results in the maximum PEEQ along the depth from the surface and the maximum plastic deformation zone. Concluded from above description, the surface roughness, residual stress and PEEQ do not monotonically increase with increasing shot size. According to Cao et al.[43], the shot diameter D and vertical impact velocity have a combined action on the surface roughness. Hence, in our analysis, shot size affects the distribution of impact ver-

tical velocity and the shot size and impact vertical velocity distribution work together to affect the impact kinetic energy of the SMAT system, which affects the FEM simulation result.

4. Conclusions

In this paper, a sequential DEM-FEM modelling method has been developed to simulate surface mechanical attrition treatment processes. The proposed method makes use of the statistical results from DEM simulations for shot dynamics, whereby simulations becomes more realistic than if distributions of impact angle and velocity were assumed random. The effect of impact number, impact angle distribution and shot size on the treatment results have been investigated and discussed. According to the results, the following conclusions can be drawn:

(1) Through a series of parametric study on the statistical distributions of impact dynamics, we found that a broader impact angle distribution increases the surface roughness, and also decreases the residual stress and equivalent plastic strain after full coverage. Whilst the order of the impact sequence was also investigated, and it was shown that the shot sequence has no effect on the simulation results.
(2) Using different shot sizes can introduce variations in distribution of vertical velocity and resulting surface roughness. Our DEM-FEM simulations shown that residual stress and equivalent plastic strain of treated target are affected by the impact kinetic energy of the SMAT system.
(3) The evolutions of the resulting surface profile, residual stress, plastic strain and hardness have been demonstrated in the simulation. With the increase of processing time, different development stages of these surface properties can be captured, where the transitions can be found for given coverages of shot impacts. These numerical predictions of mechanical properties have been further compared with available experimental data, showing good qualitative agreements.

The advantages of this proposed numerical framework have been demonstrated by the capability of predicting time evolution of the surface properties during SMAT processes, relying on the material and geometrical parameters, as well as, the operational conditions. This warrants future studies on optimizing the SMAT processes for tailored surface properties by implementing the sequential DEM-FEM method.

Declaration of Competing Interest

The authors declare that they have no known competing financial interests or personal relationships that could have appeared to influence the work reported in this paper.

CRediT authorship contribution statement

Yongmei Zhang: Conceptualization, Methodology, Investigation, Formal analysis, Visualization, Writing - original draft. **Gwénaëlle Proust:** Supervision, Conceptualization, Methodology, Investigation, Writing - review & editing. **Delphine Retraint:** Investigation, Writing - review & editing. **Huamiao Wang:** Investigation, Writing - review & editing. **Yixiang Gan:** Supervision, Conceptualization, Methodology, Investigation, Writing - review & editing.

Acknowledgements

This work was financially supported by The University of Sydney SOAR Fellowship. The authors acknowledge the support from USYD-SJTU Partnership Collaboration Awards. GP acknowledges the UTT for providing financial support for her stay at the ICD/LASMIS. This research was undertaken with the assistance of resources and services from the HPC service at The University of Sydney.

References

[1] Fang TH, Li WL, Tao NR, Lu K. Revealing extraordinary intrinsic tensile plasticity in gradient nano-grained copper. Science 2011;331:1587–90. doi:10.1126/science.1200177.
[2] Cao SC, Liu J, Zhu L, Li L, Dao M, Lu J, Ritchie RO. Nature-Inspired Hierarchical Steels. Sci Rep 2018;8:5088. doi:10.1038/s41598-018-23358-7.
[3] Umemoto M. Nanocrystallization of Steels by Severe Plastic Deformation. Mater Trans 2003;44:1900–11. doi:10.2320/matertrans.44.1900.
[4] Pakieła Z, Garbacz H, Lewandowska M, Druzycka-Wiencek A, Suś-Ryszkowska M, Zieliński W, Kurzydłowski KJ. Structure and properties of nanomaterials produced by severe plastic deformation. Nukleonika 2006;51:S19–25.
[5] Wang X, Li YS, Zhang Q, Zhao YH, Zhu YT. Gradient Structured Copper by Rotationally Accelerated Shot Peening. J Mater Sci Technol 2017;33:758–61. doi:10.1016/j.jmst.2016.11.006.
[6] Balusamy T, Kumar S, Narayanan TSNS. Effect of surface nanocrystallization on the corrosion behaviour of AISI 409 stainless steel. Corros Sci 2010;52:3826–34. doi:10.1016/j.corsci.2010.07.004.
[7] Antunes RA, de Oliveira MC. Corrosion fatigue of biomedical metallic alloys: mechanisms and mitigation. Acta Biomater 2012;8:937–62. doi:10.1016/j.actbio.2011.09.012.
[8] Teoh SH. Fatigue of biomaterials: a review. Int J Fatigue 2000;22:825–37. doi:10.1016/S0142-1123(00)00052-9.
[9] Brent Bankston A, Faris PM, Michael Keating E, Ritter MA. Polyethylene wear in total hip arthroplasty in patient-matched groups. J. Arthroplasty 1993;8:315–22. doi:10.1016/S0883-5403(06)80095-1.
[10] Hammersley G, Hackel LA, Harris F. Surface prestressing to improve fatigue strength of components by laser shot peening. Opt Lasers Eng 2000;34:327–37. doi:10.1016/S0143-8166(00)00083-X.
[11] Ke LJ. Surface nanocrystallization (SNC) of metallic materials-presentation of the concept behind a new approach. J Mater Sci Technol 1999;15:193.
[12] Mai SP, Wen CS, Lu J. Surface-modified steel sheets and corrugated panels in three-point bending. Int. J. Mech. Sci. 2018;142-143:10–20. doi:10.1016/j.ijmecsci.2018.04.024.
[13] Tao NR, Sui ML, Lu J, Lua K. Surface nanocrystallization of iron induced by ultrasonic shot peening. Nanostruct Mater 1999;11:433–40. doi:10.1016/S0965-9773(99)00324-4.
[14] Liu G, Lu J, Lu K. Surface nanocrystallization of 316L stainless steel induced by ultrasonic shot peening. MAT SCI ENG A-STRUCT 2000;286:91–5. doi:10.1016/S0921-5093(00)00686-9.
[15] Tao NR, Wang ZB, Tong WP, Sui ML, Lu J, Lu K. An investigation of surface nanocrystallization mechanism in Fe induced by surface mechanical attrition treatment. Acta Mater 2002;50:4603–16. doi:10.1016/S1359-6454(02)00310-5.
[16] Wu Y, Guelorget B, Sun Z, Déturche R, Retraint D. Characterization of gradient properties generated by SMAT for a biomedical grade 316L stainless steel. MATER CHARACT 2019;155:109788. doi:10.1016/j.matchar.2019.109788.
[17] Katti KS. Biomaterials in total joint replacement. Colloids Surf B Biointerfaces 2004;39:133–42. doi:10.1016/j.colsurfb.2003.12.002.
[18] Kohn DH. Metals in medical applications. Curr Opin Solid State Mater Sci 1998;3:309–16. doi:10.1016/S1359-0286(98)80107-1.
[19] Hermawan H, Ramdan D, Djuansjah JRP. Metals for Biomedical Applications. In: Fazel-Rezai R, editor. Biomedical Engineering - From Theory to Applications. Rijeka: InTech; 2011. p. 40–8.
[20] Semlitsch M, Willert HG. Properties of implant alloys for artificial hip joints. Med Biol Eng Comput 1980;18:511–20. doi:10.1007/bf02443329.
[21] Roland T, Retraint D, Lu K, Lu J. Enhanced mechanical behavior of a nanocrystallised stainless steel and its thermal stability. MAT SCI ENG A-STRUCT 2007;445-446:281–8. doi:10.1016/j.msea.2006.09.041.
[22] Samih Y, Beausir B, Bolle B, Grosdidier T. In-depth quantitative analysis of the microstructures produced by Surface Mechanical Attrition Treatment (SMAT). MATER CHARACT 2013;83:129–38. doi:10.1016/j.matchar.2013.06.006.
[23] Proust G, Trimby P, Piazolo S, Retraint D. Characterization of Ultra-fine Grained and Nanocrystalline Materials Using Transmission Kikuchi Diffraction. J. Vis. Exp. 2017:e55506. doi:10.3791/55506.
[24] Proust G, Retraint D, Chemkhi M, Roos A, Demangel C. Electron Backscatter Diffraction and Transmission Kikuchi Diffraction Analysis of an Austenitic Stainless Steel Subjected to Surface Mechanical Attrition Treatment and Plasma Nitriding. Microsc. Microanal. 2015;21:919–26. doi:10.1017/S1431927615000793.
[25] Hu J, Shi YN, Sauvage X, Sha G, Lu K. Grain boundary stability governs hardening and softening in extremely fine nanograined metals. Science 2017;355:1292–6. doi:10.1126/science.aal5166.
[26] Misra RDK, Nune C, Pesacreta TC, Somani MC, Karjalainen LP. Understanding the impact of grain structure in austenitic stainless steel from a nanograined regime to a coarse-grained regime on osteoblast functions using a novel metal deformation–annealing sequence. Acta Biomater 2013;9:6245–58. doi:10.1016/j.actbio.2012.12.003.
[27] Yin F, Xu R, Hu S, Zhao K, Yang S, Kuang S, Li Q, Han Q. Enhanced Mechanical and Biological Performance of an Extremely Fine Nanograined 316L Stainless Steel Cell–Substrate Interface Fabricated by Ultrasonic Shot Peening. ACS Biomater. Sci. Eng. 2018. doi:10.1021/acsbiomaterials.8b00173.
[28] Azadmanjiri J, Berndt CC, Kapoor A, Wen C. Development of Surface Nano-Crystallization in Alloys by Surface Mechanical Attrition Treatment (SMAT). Crit. Rev. Solid State Mater. Sci. 2015;40:164–81. doi:10.1080/10408436.2014.978446.
[29] Estrin Y, Vinogradov A. Extreme grain refinement by severe plastic deformation: A wealth of challenging science. Acta Mater 2013;61:782–817. doi:10.1016/j.actamat.2012.10.038.

[30] Roland T, Retraint D, Lu K, Lu J. Generation of Nanostructures on 316L Stainless Steel and Its Effect on Mechanical Behavior. Mater. Sci. Forum 2005;490-491:625–30. doi:10.4028/www.scientific.net/MSF.490-491.625.
[31] Chan HL, Ruan HH, Chen AY, Lu J. Optimization of the strain rate to achieve exceptional mechanical properties of 304 stainless steel using high speed ultrasonic surface mechanical attrition treatment. Acta Mater 2010;58:5086–96. doi:10.1016/j.actamat.2010.05.044.
[32] Zhou J, Retraint D, Sun Z, Kanouté P. Comparative study of the effects of surface mechanical attrition treatment and conventional shot peening on low cycle fatigue of a 316L stainless steel. Surf. Coat. Technol. 2018;349:556–66. doi:10.1016/j.surfcoat.2018.06.041.
[33] Wang C, Wang L, Wang X, Xu Y. Numerical study of grain refinement induced by severe shot peening. Int. J. Mech. Sci. 2018;146-147:280–94. doi:10.1016/j.ijmecsci.2018.08.005.
[34] Bahl S, Suwas S, Ungàr T, Chatterjee K. Elucidating microstructural evolution and strengthening mechanisms in nanocrystalline surface induced by surface mechanical attrition treatment of stainless steel. Acta Mater 2017;122:138–51. doi:10.1016/j.actamat.2016.09.041.
[35] Bahl S, Shreyas P, Trishul MA, Suwas S, Chatterjee K. Enhancing the mechanical and biological performance of a metallic biomaterial for orthopedic applications through changes in the surface oxide layer by nanocrystalline surface modification. Nanoscale 2015;7:7704–16. doi:10.1039/c5nr00574d.
[36] Chaise T, Li J, Nélias D, Kubler R, Taheri S, Douchet G, Robin V, Gilles P. Modelling of multiple impacts for the prediction of distortions and residual stresses induced by ultrasonic shot peening (USP). J Mater Process Technol 2012;212:2080–90. doi:10.1016/j.jmatprotec.2012.05.005.
[37] Yin F, Hu S, Hua L, Wang X, Suslov S, Han Q. Surface Nanocrystallization and Numerical Modeling of Low Carbon Steel by Means of Ultrasonic Shot Peening. Metall Mater Trans A Phys Metall Mater Sci 2015;46:1253–61. doi:10.1007/s11661-014-2689-z.
[38] Yin F, Hua L, Wang X, Rakita M, Han Q. Numerical modelling and experimental approach for surface morphology evaluation during ultrasonic shot peening. Comput. Mater. Sci. 2014;92:28–35. doi:10.1016/j.commatsci.2014.05.011.
[39] Zhang XC, Lu J, Shi SQ. A Computational Study of Plastic Deformation in AISI 304 Induced by Surface Mechanical Attrition Treatment. Mech. Adv. Mater. Struct. 2011;18:572–7. doi:10.1080/15376494.2011.621828.
[40] Meguid SA, Shagal G, Stranart JC. Finite element modelling of shot-peening residual stresses. J Mater Process Technol 1999;92-93:401–4. doi:10.1016/s0924-0136(99)00153-3.
[41] Meguid SA, Shagal G, Stranart JC. 3D FE analysis of peening of strain-rate sensitive materials using multiple impingement model. Int J Impact Eng 2002;27:119–34. doi:10.1016/S0734-743X(01)00043-4.
[42] Pham TQ, Khun NW, Butler DL. New approach to estimate coverage parameter in 3D FEM shot peening simulation. Surf. Eng. 2017;33:687–95. doi:10.1080/02670844.2016.1274536.
[43] Cao SC, Zhang X, Lu J, Wang Y, Shi S-Q, Ritchie RO. Predicting surface deformation during mechanical attrition of metallic alloys. NPJ Comput. Mater. 2019;5. doi:10.1038/s41524-019-0171-6.
[44] Gangaraj SMH, Guagliano M, Farrahi GH. An approach to relate shot peening finite element simulation to the actual coverage. Surf. Coat. Technol. 2014;243:39–45. doi:10.1016/j.surfcoat.2012.03.057.
[45] Hassani-Gangaraj SM, Cho KS, Voigt HJL, Guagliano M, Schuh CA. Experimental assessment and simulation of surface nanocrystallization by severe shot peening. Acta Mater 2015;97:105–15. doi:10.1016/j.actamat.2015.06.054.
[46] Badreddine J, Rouhaud E, Micoulaut M, Remy S. Simulation of shot dynamics for ultrasonic shot peening: Effects of process parameters. Int. J. Mech. Sci. 2014;82:179–90. doi:10.1016/j.ijmecsci.2014.03.006.
[47] Han K, Peric D, Crook AJL, Owen DRJ. A combined finite/discrete element simulation of shot peening processes – Part I: studies on 2D interaction laws. ENG COMPUTATION 2000;17:593–620. doi:10.1108/02644400010339798.
[48] Tu F, Delbergue D, Miao H, Klotz T, Brochu M, Bocher P, Levesque M. A sequential DEM-FEM coupling method for shot peening simulation. Surf. Coat. Technol. 2017;319:200–12. doi:10.1016/j.surfcoat.2017.03.035.
[49] Zhang Y, Proust G, Retraint D, Wang H, Gan Y. Discrete element simulation of surface mechanical attrition treatment with rough-surface sonotrode. Int. J. Mech. Sci. 2019;161-162:105060. doi:10.1016/j.ijmecsci.2019.105060.
[50] Bagherifard S, Ghelichi R, Guagliano M. A numerical model of severe shot peening (SSP) to predict the generation of a nanostructured surface layer of material. Surf. Coat. Technol. 2010;204:4081–90. doi:10.1016/j.surfcoat.2010.05.035.
[51] Frija M, Hassine T, Fathallah R, Bouraoui C, Dogui A. Finite element modelling of shot peening process: Prediction of the compressive residual stresses, the plastic deformations and the surface integrity. MAT SCI ENG A-STRUCT 2006;426:173–80. doi:10.1016/j.msea.2006.03.097.
[52] Montross C. Laser shock processing and its effects on microstructure and properties of metal alloys: a review. Int J Fatigue 2002;24:1021–36. doi:10.1016/s0142-1123(02)00022-1.
[53] Ghasemi A, Hassani-Gangaraj SM, Mahmoudi AH, Farrahi GH, Guagliano M. Shot peening coverage effect on residual stress profile by FE random impact analysis. Surf. Eng. 2016;32:861–70. doi:10.1080/02670844.2016.1192336.
[54] Meo M, Vignjevic R. Finite element analysis of residual stress induced by shot peening process. Adv. Eng. Softw., 2003;34:569–75. doi:10.1016/s0965-9978(03)00063-2.
[55] Miao HY, Larose S, Perron C, Lévesque M. On the potential applications of a 3D random finite element model for the simulation of shot peening. Adv. Eng. Softw. 2009;40:1023–38. doi:10.1016/j.advengsoft.2009.03.013.
[56] ABAQUS I. ABAQUS Analysis User's Manual, Version 6.6. Providence, RI: Dassault Systèmes Simulia Corp; 2006.
[57] Kim T, Lee H, Hyun HC, Jung S. A simple but effective FE model with plastic shot for evaluation of peening residual stress and its experimental validation. MAT SCI ENG A-STRUCT 2011;528:5945–54. doi:10.1016/j.msea.2011.04.012.
[58] Dai K, Villegas J, Stone Z, Shaw L. Finite element modeling of the surface roughness of 5052 Al alloy subjected to a surface severe plastic deformation process. Acta Mater 2004;52:5771–82. doi:10.1016/j.actamat.2004.08.031.
[59] Jiang H, Liu L, Zhou L, Lu J. Residual stresses measurement with hole-drilling method on 6,061 aluminum under SMAT treatment. World Journal of Engineering 2012;9:487–92. doi:10.1260/1708-5284.9.6.487.
[60] Yin F, Cheng GJ, Xu R, Zhao K, Li Q, Jian J, Hu S, Sun S, An L, Han Q. Ultrastrong nanocrystalline stainless steel and its Hall-Petch relationship in the nanoscale. Scripta Materialia 2018;155:26–31. doi:10.1016/j.scriptamat.2018.06.014.
[61] Kondi Maliwemu EU, Malau V, Iswanto PT. Effect of Shot Peening in Different Shot Distance and Shot Angle on Surface Morphology, Surface Roughness and Surface Hardness of 316L Biomaterial. IOP CONF. SER. MATER. SCI. ENG 2018;299:012051. doi:10.1088/1757-899x/299/1/012051.
[62] Nordin E, Alfredsson B. Experimental Investigation of Shot Peening on Case Hardened SS2506 Gear Steel. Exp Tech 2017;41:433–51. doi:10.1007/s40799-017-0183-4.